This is an open access article published under an ACS AuthorChoice License, which permits copying and redistribution of the article or any adaptations for non-commercial purposes.

ACS central science

Research Article

http://pubs.acs.org/journal/acscii

Tunable Multiscale Nanoparticle Ordering by Polymer Crystallization

Dan Zhao,[†] Vianney Gimenez-Pinto,[†] Andrew M. Jimenez,[†] Longxi Zhao,[†] Jacques Jestin,[*,†,‡] Sanat K. Kumar,[*,†] Brooke Kuei,[§] Enrique D. Gomez,[§] Aditya Shanker Prasad,[∥] Linda S. Schadler,[∥] Mohammad M. Khani,[⊥] and Brian C. Benicewicz[⊥]

[†]Department of Chemical Engineering, Columbia University, New York, New York 10027, United States

[‡]Laboratoire Léon Brillouin, CEA Saclay, 91191 Gif-sur-Yvette Cedex, France

[§]Department of Chemical Engineering, Pennsylvania State University, University Park, Pennsylvania 16802, United States

[∥]Department of Materials Science and Engineering, Rensselaer Polytechnic Institute, Troy, New York 12180, United States

[⊥]Department of Chemistry and Biochemistry, University of South Carolina, Columbia, South Carolina 29208, United States

Supporting Information

ABSTRACT: While ∼75% of commercially utilized polymers are semicrystalline, the generally low mechanical modulus of these materials, especially for those possessing a glass transition temperature below room temperature, restricts their use for structural applications. Our focus in this paper is to address this deficiency through the controlled, multiscale assembly of nanoparticles (NPs), in particular by leveraging the kinetics of polymer crystallization. This process yields a multiscale NP structure that is templated by the lamellar semicrystalline polymer morphology and spans NPs engulfed by the growing crystals, NPs ordered into layers in the interlamellar zone [spacing of O (10−100 nm)], and NPs assembled into fractal objects at the interfibrillar scale, O (1−10 μm). The relative fraction of NPs in this hierarchy is readily manipulated by the crystallization speed. Adding NPs usually increases the Young's modulus of the polymer, but the effects of multiscale ordering are nearly an order of magnitude larger than those for a state where the NPs are not ordered, i.e., randomly dispersed in the matrix. Since the material's fracture toughness remains practically unaffected in this process, this assembly strategy allows us to create high modulus materials that retain the attractive high toughness and low density of polymers.

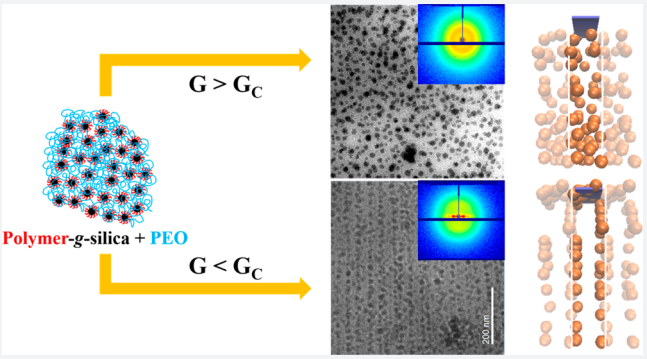

INTRODUCTION

It is well-known that varying nanoparticle (NP) dispersion in polymer, metal, or ceramic matrices can dramatically improve material properties.[1−5] While uniform NP spatial distribution is usually the focus,[4,6] many situations benefit from spatially nonuniform, anisotropic NP organization. Nature teaches us that hierarchical NP ordering, as achieved in the case of nacre (a hybrid composed of 95% inorganic aragonite and 5% crystalline polymer, e.g., chitin), strongly improves mechanical properties relative to the building blocks. Specifically, a nanoscale ∼10 nm thick crystalline biopolymer layer mediates parallel layers of aragonite, forming "bricks", which subsequently assemble into "brick-and-mortar" superstructures at the micrometer scale and larger.[7,8] While the spontaneous assembly of NPs into a hierarchy of scales in a polymer host has been a "holy grail" in nanoscience, there is currently no established method to achieve this goal.[9−14]

We fill this critical void by assembling NPs simultaneously into three scales in the polymer-rich regime by leveraging the hierarchical structure of the lamellar semicrystalline polymer morphology: (i) NPs that are engulfed by the crystallization front and remain spatially well-dispersed; (ii) NPs assembled into sheets at the O (10−100 nm) scale, and (iii) NP aggregates at the 1−10 μm scale (Scheme 1A). The partitioning of the NPs into the three zones is controlled by the crystal growth rate. This assembly causes a dramatic improvement in the modulus of the material while retaining the attractive large toughness and low density of the pure semicrystalline polymer.

RESULTS AND DISCUSSION

Polymer melt crystallization typically yields an anisotropic lamellar morphology where oriented chain stems are added along the spherulite perimeter producing crystal growth in all three directions (Scheme 1B).[15] The resulting crystal dimensions are quite different in the lamellar (i, 10−100 nm), fibrillar (g, μm), and spherulitic (G, μ-cm) directions. We first define a critical growth velocity G_c above which most of the initially well-dispersed NPs are engulfed by the growing crystal and thus remain isotropically distributed in the polymer

Received: April 12, 2017
Published: June 7, 2017

 © 2017 American Chemical Society

DOI: 10.1021/acscentsci.7b00157
ACS Cent. Sci. 2017, 3, 751−758

Scheme 1. (A) The Hierarchical NP (Blue Circles) Structure in a Semicrystalline Polymer Matrix.[a] (B) Schematic for Polymer Surface Nucleation and the Growth Front, where "*g*" is the Lateral Growth Direction, "*i*" is the Secondary Nucleation Direction, and "*G*" is the Spherulite Growth Direction[b]

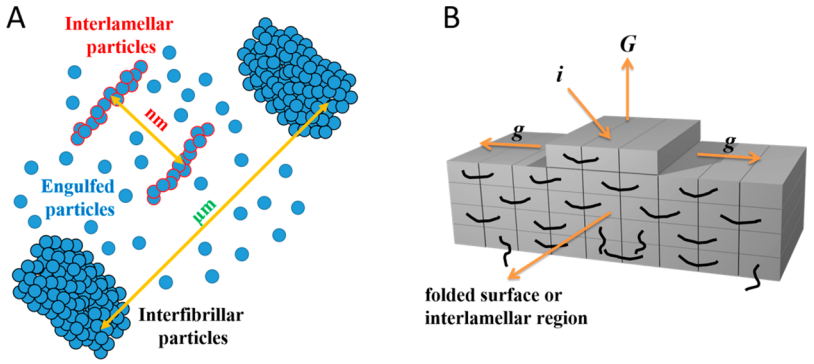

[a]The polymer chains are not shown for clarity. [b]Black lines are connections between crystal stems.

(Figures 1A and 1B). While G_c can be defined in several ways, for simplicity we compare the time scale for NP diffusion away from the growing crystal, $\tau_D = a^2/D$, to that for crystal growth, $\tau_G = a/G$,[16−18] where a is the crystal lattice spacing and D is the NP diffusion constant. Applying the Stokes−Einstein equation yields $G_c = \frac{kT}{6\pi\eta Ra}$; k is Boltzmann's constant, T is the temperature, R is the NP radius, and η is the medium viscosity. (The Stokes−Einstein relationship can underestimate the diffusion coefficient of 10 nm sized NP in a polymer melt;[19,20] however we deem this approach appropriate for illustrating the phenomena of interest in this system.) Thus, $G_c \sim 0.01-1$ μm/s for NPs of $R \sim 10$ nm is obtained in typical polymeric materials.[21]

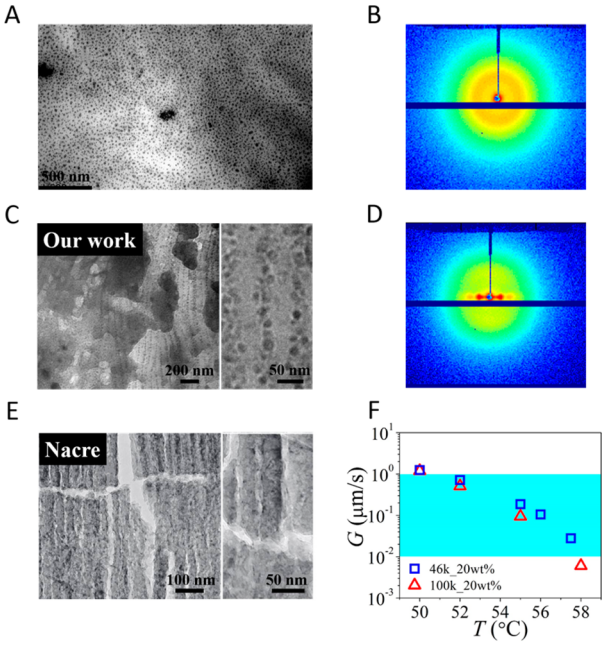

Figure 1. TEM micrographs of 40 wt % PMA-*g*-silica NPs in 100 kg mol^{-1} PEO: (A) fast crystallization, quenched in liquid nitrogen and (C) slow crystallization, isothermally crystallized at 58 °C for 7 days. 2-D SAXS pattern for 20 wt % PMMA-*g*-silica in 46 kg mol^{-1} PEO (B) quenched by liquid nitrogen from the melt and (D) isothermally crystallized at 57.5 °C for 7 days. Note that the orientation of the anisotropic scattering pattern in panel D is purely random. (E) The nanoscale structure in nacre.[8] (F) Spherulite growth rate vs temperature for 46 or 100 kg mol^{-1} PEO loaded with 20 wt % PMMA-*g*-silica NP. Data points are averaged over at least five spherulites from different regions of the sample, and the resulting error bars are comparable to symbol size. The region highlighted in light green indicates the critical spherulite growth rate (i.e., $G_c \sim 0.01-1$ μm/s).

We show here that, while the NPs are almost completely engulfed for $G > G_c$, they are progressively expelled from the crystal and ordered into the three hierarchical scales in the lamellar morphology for $G < G_c$ (Scheme 1A, Figures 1C and 1D). Notably, the nanoscale NP organization is structurally similar to that of nacre on comparable length scales (Figure 1E). For rates just below G_c we conjecture that the system loses less free energy by placing NPs into the interlamellar regions (where they are the most confined) than having the growing crystal front "push" the NPs all the way to the (interspherulitic) grain boundaries. The NP ordering in this situation is thus templated by the lamellar morphology resulting in parallel NP sheets with the desired $O(10-100$ nm) spacing. As G is decreased further, the fraction of engulfed particles decreases, and more NPs are placed in regions where they are progressively less confined, namely, the interlamellar region followed by the interfibrillar and then the interspherulitic zone. This protocol allows us to access multiscale NP ordering relevant to biomimetics in a facile manner by variations in the crystal growth rate.[22]

Experimental Systems. Two different poly(ethylene oxide) (PEO) melts (molecular weight M_w = 100 kg mol^{-1} and 46 kg mol^{-1}, respectively) are well-mixed with polymer-grafted-silica NPs. The spherical silica NP core diameter is 14 ± 4 nm, and the polymer brush is either poly(methyl methacrylate) (PMMA, grafting density, σ = 0.24 chains/nm^2, and M_w = 28 kg mol^{-1}) or poly(methyl acrylate) (PMA, σ = 0.43 chains/nm^2, and M_w = 62 kg mol^{-1}).[23,24] Unless otherwise noted, the PEO has a M_w = 100 kg mol^{-1} and the particle is PMMA-*g*-silica. Also, the reported NP loading includes the brush, e.g., for the 20 wt % PMMA-*g*-silica, the volume percentage of silica core is ∼3.5% (Table S1 in Supporting Information). Additionally, note that all the "S#" tables and figures in the text below are provided in the Supporting Information.

Proving Miscibility in the Melt State. Transmission electron microscopy (TEM, Figure S1a for PMMA-*g*-silica and

DOI: 10.1021/acscentsci.7b00157
ACS Cent. Sci. 2017, 3, 751−758

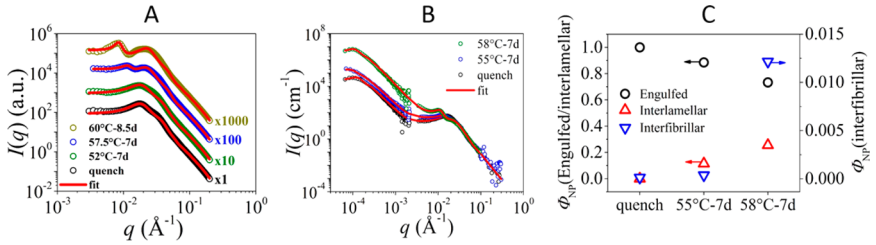

Figure 2. (A) 1-D SAXS traces for 20 wt % PMMA-*g*-silica in 100 kg mol^{-1} PEO isothermally crystallized at different temperatures (°C) for various time periods (days). The curves are vertically shifted for clarity. Also note that each scattering trace is an average of scattering from at least five spots in the same sample. (B) 1-D SANS/VSANS traces for 20 wt % PMMA-*g*-silica in 100 kg mol^{-1} PEO isothermally crystallized at different temperatures (°C) for various time periods (days). Red solid lines in both panels A and B represent best fits to polydisperse core−shell and fractal cluster form factors coupled to the Percus−Yevick structure factors, see the text for more details. (C) Normalized volume fraction of NPs (Φ_{NP}) located at different length scales (engulfed, interlamellar, or interfibrillar) extracted from panel B.

Figure 1A for PMA-*g*-silica) and small angle X-ray scattering (SAXS, Figure S2 and Table S1) confirm individual NP distribution in the polymer after rapid quenching with liquid nitrogen. No remarkable difference is seen in the SAXS profiles between the molten and the quenched samples, confirming that quenching did not affect the NP dispersion (Figure S3). Analysis of the SAXS data at 10 wt % NP yields the median silica core size ($R \sim 6.3$ nm, log-normal polydispersity of 0.28). This is close to the accepted value ($R = 7 \pm 2$ nm).

At higher NP concentrations the interparticle surface-to-surface distance (h_{s-s}), obtained by fitting the SAXS data to the hard-sphere Percus−Yevick model (Figure S2e), is essentially that expected assuming random NP dispersion. Linear rheology shows that the temperature dependent shift factors for the melt mixtures are intermediate between those for pure PEO and PMMA (Figure S4). Based on these multiple results, we conclude that the NPs are homogeneously dispersed in the molten matrix, probably because PEO and PMMA are thermodynamically compatible.[23] Similarly, the PMA-*g*-silica NPs are also well-mixed with the PEO melts (Figure 1A).[24]

A series of melts were quenched to different temperatures, thus systematically varying G, and isothermally crystallized for different periods of time. The PEO crystal unit cell and mechanism of crystallization are apparently not significantly affected by the NPs even at 20 wt % loading (Figures S5b and S5c).[25] However, the NPs reduce G (Figures S5a and S6, Table S2) for larger loadings presumably due to confinement (Figures S7 and S8). Therefore, by varying NP content or crystallization temperature, we can make G larger or smaller than G_c (Figure 1F). Additional facts about the effect of NP on polymer crystallization are provided in the Supporting Information.

NP Organization Driven by Polymer Crystallization. We next examine the role of isothermal polymer crystallization on NP assembly. For $G > G_c$ (e.g., isothermal crystallization at 52 °C), the SAXS pattern is essentially the same as that of the quenched sample (Figure 2A). The NPs are apparently engulfed by the growing crystal front and do not show large changes in their spatial dispersion.[25] SAXS and small angle neutron scattering (SANS, Figures S9 and S10) verify these conclusions and provide detailed insights. At 20 wt % NP, the average h_{s-s}, the face-to-face separation between the NPs is essentially unchanged even after 7 d crystallization (Figure S10). In contrast, h_{s-s} for the 40 wt % NP is reduced after 4 h crystallization, beyond which it is essentially equal to zero. No significant changes are found for the 60 wt % sample where $h_{s-s} \approx 0$ at all times (Figure S9). These results strongly suggest that, even though the NPs tend to locally move until they come into contact, no large-scale ordering emerges. These findings are unrelated to the glass transition temperature T_g of PMMA (~110 °C), since PMA ($T_g \sim 14$ °C) grafted NPs behave similarly.

However, with increasing crystallization temperature (or lowering G, e.g., $T > 55$ °C), we see three peaks in the scattering patterns (Figures 2A and 2B). The interparticle correlation peak (highest q) shifts to larger q upon crystallization (from ~0.017 Å^{-1} to ~0.023 Å^{-1}, Figures S10 and S11), suggesting that the NPs locally approach each other. The intermediate $q \approx 0.01$ Å^{-1} peak, corresponding to a correlation distance of ~63 nm, is associated with one of the new NP structures formed by crystallization at 58 °C, where $G \sim 6 \times 10^{-3}$ μm/s for 20 wt % PMMA-*g*-silica in 100 kg mol^{-1} PEO. TEM and scattering show that the NPs are aligned into parallel sheet-like structures (Figures 1C, 1D, and S1B). Using a PMMA-*g*-silica NP diameter of ~23 nm and the known PEO long period of ~41 nm at 58 °C (Figure S12) verifies this structural assignment. Fourier transforms reiterate the anisotropic NP spatial distribution (inset of Figure S1B). The kinetics of the formation of these structures speeds up when PEO with a smaller molecular weight (e.g., 46 kg mol^{-1}) or NPs with a larger mobility (PMA-*g*-silica) are used (Figures S11 and 1C). Remarkably, this nanoscale NP ordering strongly resembles that observed in nacre at the nanoscale, except that nacre is ~95% inorganic while our materials are ~97% organic (Figure 1E). Very small angle neutron scattering (VSANS, Figure 2B) reveals a third peak at an even lower q (~10^{-4} Å^{-1}), indicating a population of NPs ordered at a larger scale (~6 μm), presumably corresponding to the interfibrillar region.

To model the scattering curves we used three NP populations: (I) primary "engulfed" NPs, (II) an "interlamellar" population, and (III) an "interfibrillar" component. For each population, a polydisperse form factor and its associated structure factor are adopted, as given by

$$I(q) = \varphi_1 P_1(q)\, S_1(q) + \varphi_2 P_2(q)\, S_2(q) + \varphi_3 P_3(q)\, S_3(q) \quad (1)$$

where φ, $P(q)$, and $S(q)$ are the volume fraction, form factor, and structure factor of the NP structures. "1", "2", and "3" correspond respectively to the structure of populations I, II, and III. Specifically, $P_1(q)$ is the form factor of a single polymer grafted NP modeled with a polydisperse spherical core−shell (note that, in neutron scattering, the contrast of the shell is close to that of the matrix, thus making the shell nearly invisible) and $S_1(q)$ is the structural correlation between single particles; $P_2(q)$ is compact aggregates of several primary NPs

DOI: 10.1021/acscentsci.7b00157
ACS Cent. Sci. 2017, 3, 751−758

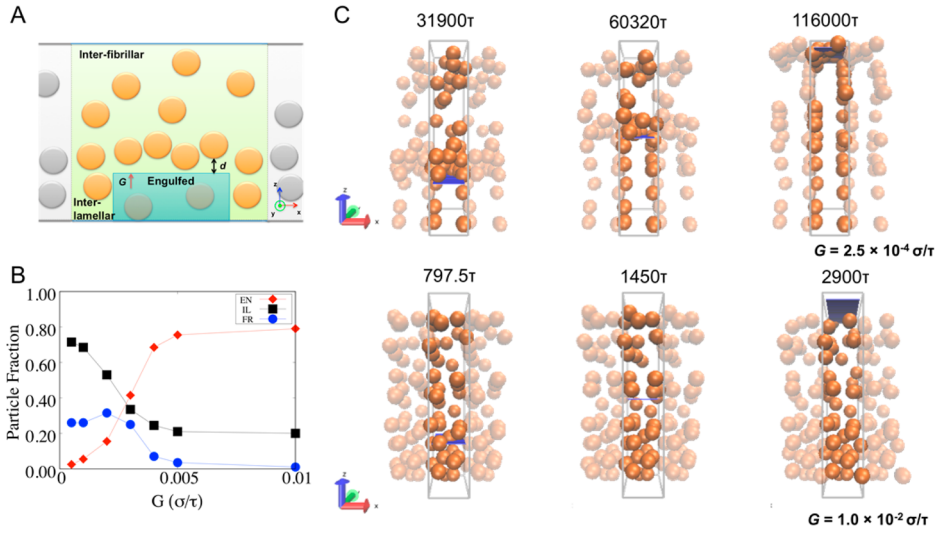

Figure 3. Molecular dynamics simulations on NP ordering by a crystallizing front of fixed thickness. (A) Simulation model schematics. (B) Particle fraction inside each region as a function of front velocity G. "EN", "IL", and "FR" correspond respectively to engulfed, interlamellar, and free (interfibrillar) regions. Note that the apparent local maximum in the interfibrillar particle fraction falls within simulation uncertainties due to the small number of particles (40) in the simulations. Use of larger numbers of NPs serves to eliminate this maximum. (C) From left to right: initial, intermediate, and final snapshots of the simulation. Top: Anisotropic NP organization observed at small $G = 2.5 \times 10^{-4}\sigma/\tau$. Bottom: Isotropic NP organization at large front velocities $G = 1.0 \times 10^{-2}\sigma/\tau$.

modeled with a core−shell of larger effective radius within the layers, and $S_2(q)$ represents the interlayer correlations; $P_3(q)$, corresponding to the particle structure in the interfibrillar region, is modeled by fractal clusters, and $S_3(q)$ is the associated structure factor. $S_1(q)$, $S_2(q)$, and $S_3(q)$ are modeled by the hard-sphere Percus−Yevick structure factor. Note that this model assumes no correlation between different populations. Additionally, we have also used a rod-like form factor (rods made up of spherical NPs) for $P_2(q)$, but no significant improvements over the fittings were achieved, and similar results were obtained. Moreover, we only observed strongly anisotropic scattering in the 46 kg mol^{-1} based samples (Figure 1D), in which case the form and structure factor cannot be decoupled. However, for those in 100 kg mol^{-1} PEO, the scattering pattern is isotropic in both X-ray and neutron beams, and hence the model we propose here is valid. For quantitative analysis (Figure 2C), we relied on the neutron scattering data instead of the X-ray scattering, as in the latter case the beam size is comparable to or maybe even smaller than that of one spherulite. Therefore, the scattering pattern could not be representative of the entire sample. In contrast, in neutron scattering, where the beam size is much larger, the sample scattering is always isotropic and also should well represent the ensemble structure of the entire sample. The fitting results obtained in this manner are presented in Figure 2C and also provided in Table S3.

Our modeling results illustrate two important facts: (i) The average interlamellar distance can be easily tuned by controlling the crystallization temperature (Figure 2A). For example, we clearly observe layered NP structures upon crystallization at 60 °C for 8.5 days (Figures S1C and S1D), with a SAXS determined interlamellar correlation length of ∼70 nm = ∼23 nm + ∼50 nm (PEO long period at this temperature, Figure S12), while at 57.5 °C the distance between layered particles is reduced to ∼57 nm. Moreover, this average interlayer distance apparently increases with NP content (Figure S13). For example, in the samples with PMA-*g*-silica in 100 kg mol^{-1} PEO, the mean interlamellar distance estimated from SAXS is ∼71 nm and ∼94 nm, respectively, for the 40 and 60 wt % samples at 58 °C. These SAXS findings are in good agreement with TEM estimates (e.g., for the 40 wt % loading we find a spacing of ∼75 nm, Figure 1C). (ii) The fraction of NPs in the interlamellar zone increases as G decreases. We find that all the NPs are engulfed in the quenched sample and also at 52 °C (Figures 2A, S10, and S11); ∼15% of the NPs (or ∼0.5 vol % silica in the sample) are interlamellar at 55 °C while it is ∼26% (or ∼0.9 vol % silica core) at 58 °C (Figure 2C). Similarly, we find no significant fraction of interfibrillar NPs at 52 °C, while ∼1% of the NPs (or ∼0.04 vol % silica core) are interfibrillar at 58 °C (Figure 2C). This clearly illustrates that decreasing G directs the NPs to be placed preferentially in the interlamellar and interfibrillar zones, rather than be engulfed.[26] Presumably, crystallizing at even lower rates will result in an increased percentage of NPs placed in the interfibrillar/interspherulitic zones.[22,27] This last inference is consistent with NP ordering by the crystallization of small molecules, e.g., ice templating, where the NPs are exclusively placed at grain boundaries for $G \ll G_c$.[12,28]

Simulations. To investigate the role of polymer crystallization on NP organization, we simulate a model that abstracts the morphology represented in Scheme 1B while retaining important details. By modeling a pillar-like moving crystal front with finite thickness (Figure 3A) in the second direction (but infinite thickness in the third direction) we can model engulfed NPs, NPs localized on the sides of the crystal ("interlamellar" particles) or NPs placed preferentially on top ("free" NPs, which are used to model the interfibrillar zone); Figure S14 show details on free particle localization ahead of the front. We can also describe the interspherulitic zone by making the pillar finite in all directions, but do not include this feature here. Additional details can be found in Materials and Methods as well as the Supporting Information. Figures 3B and 3C show representative results for the fraction of NPs localized in the three different regions vs G. At large G, the NPs are predominantly engulfed: i.e., the crystal grows so rapidly that the NPs can only reorder locally but cannot escape the growing

DOI: 10.1021/acscentsci.7b00157
ACS Cent. Sci. 2017, 3, 751−758

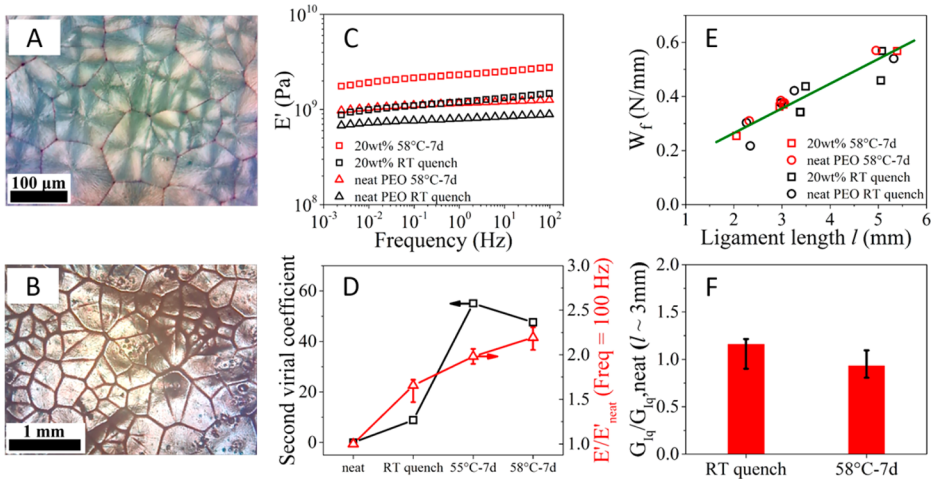

Figure 4. Optical microscopy of 20 wt % PMMA-*g*-silica NPs in 100 kg mol^{-1} PEO (A) quenched to room temperature; (B) isothermally crystallized at 58 °C for 7 days. (C) Storage modulus (E') at room temperature for samples either quenched at room temperature (RT quench) or crystallized at 58 °C for 7 days. The loss modulus and loss angle are presented in Figure S16. (D) Mechanical second virial coefficient and reinforcement ratio at 100 Hz for samples crystallized at different conditions, as indicated in the graph. (E) The specific work of fracture as a function of ligament length (i.e., the width of the sample minus the precrack depth) measured by SEN-3PB. (F) The energy release rate G_{1q} at a ligament length (l) of ∼3 mm normalized by the neat polymer crystallized at identical conditions (minimum three specimens each). We use G_{1q} since the specimen dimensions did not strictly follow ASTM plane strain criteria.

crystals. Below G_c the NPs are progressively expelled into the interlamellar and interfibrillar zones. Notice that the "transition" in behavior is gradual and that we can vary the fraction of NPs in the two zones through judicious choices of G. While the interlamellar particle fraction progressively increases as G is reduced, the interfibrillar fraction appears to show a local maximum. However, this is not a real feature since it is within the uncertainties associated with the use of a small number of particles (N = 40) in the simulation. The underpinning idea that growing fronts can "sweep" NPs along is well-accepted in the freeze casting community[26] eventually leading them to be placed in the intercrystal zone. By analogy, we propose that the NPs are swept by the crystal front and eventually end up in the interfibrillar zones under the conditions relevant to our experiments.

Consequences on Mechanical Properties. Dynamic mechanical thermal analysis (DMTA) yields the linear mechanical behavior at room temperature, and single-edge notched three-point bending tests provide fracture toughness information (SEN-3PB). We compare identically crystallized NP-loaded polymers and pure PEO samples which have comparable spherulite sizes and crystallinities (Figures 4A, 4B, and S15, Table S4).

The addition of 20 wt % well-dispersed NPs increases the 100 Hz elastic modulus (E') by a factor of ∼1.6 (Figures 4C and 4D, "RT quench"). Fitting to the Guth−Gold relationship, $E'_{disorder} = E'_{PEO}[1 + 0.67\alpha\Phi_{silica} + 1.62(\alpha\Phi_{silica})^2]$,[29] yields α = 12.5 and thus a second virial coefficient $\lim_{\Phi_{silica}\to 0} \frac{E'_{disorder} - E'_{PEO}}{E'_{PEO}\Phi_{silica}} = 8.4$. In contrast, when NPs are hierarchically organized, the E' (Figure 4D, "58°C-7d") increases by ∼2.2 relative to the pure matrix, even though only ∼26% of the NPs are interlamellar (at 55 °C this increase is ∼2.0 times). This reinforcement is fit with a linear relationship: $(E'/E'_{PEO})_{order} = (E'/E'_{PEO})_{disorder}(1 + 50\Phi_{interlamellar})$, where the $E'_{disorder}$ is discussed above. The ratio of mechanical second virial coefficients implies that ordered NPs give a (50 + 8.4)/8.4 ≈ 7-fold increase in modulus relative to the disordered analogue. This dramatic effect on the polymer's stiffness represents an important practical consequence of NP assembly.

SEN-3PB experiments enumerate the strain energy release rate, G_{1q} (Figures 4F and S17). Since the amorphous part of PEO is rubbery at room temperature, plastic deformation can cause significant energy dissipation (highly drawn fibrils on fracture surfaces, Figure S18).[30] To avoid these problems, we studied samples with a series of precrack lengths and measured the work of fracture.[31] The y-intercept in Figure 4E yields the material specific fracture toughness, while the slope gives the plastic contribution. Figures 4E and 4F consistently demonstrate that the fracture toughness is practically unaffected, independent of NP spatial order (Figure S19).

CONCLUDING REMARKS

In summary, via experiments and applicable simulations we have achieved, explained, and demonstrated the emergence of multiscale NP ordering in lamellar semicrystalline polymer matrices by tuning a single parameter, the crystallization speed. An enhanced material modulus is a direct consequence of these phenomena. Furthermore, this tunable multiscale order arises from a delicate interplay between particle mobility, confinement, and the inherently anisotropic polymer crystal morphology, which opens avenues for the development of improved polymeric materials.

MATERIALS AND METHODS

Materials and Synthesis. Tetrahydrofuran (THF, ACS agent, >99.0%) was purchased from Sigma-Aldrich. Poly(ethylene oxide) (PEO) was ordered from Scientific Polymer Products (M_w ∼ 100 kg mol^{-1}), Sigma-Aldrich (M_v = 100 kg mol^{-1}, powder), or Polymer Source (M_w = 46 kg mol^{-1}, M_w/M_n = 1.18). Poly(methyl methacrylate) (PMMA) chains were grown from the surface of spherical silica NPs (Nissan Chemical Industries, MEK-ST, with a diameter of 14 ± 4 nm), using reversible addition−fragmentation chain transfer polymerization,[32] resulting in a grafting chain molecular weight of 28 kg mol^{-1}, and a grafting density of ∼0.24 chains/nm^2.

DOI: 10.1021/acscentsci.7b00157
ACS Cent. Sci. 2017, 3, 751−758

Poly(methyl acrylate) (PMA) grafted silica NPs with a grafting chain length of 62 kg mol^{-1} and 0.43 chains/nm^2 were also synthesized. Antioxidant Irganox 1010, donated by Ciba Specialty Chemicals (now BASF Switzerland), was used to minimize thermal degradation during annealing.

Sample Preparation and Processing. The PEO (with ∼0.5 wt % Irganox relative to the mass of PEO) was dissolved in THF at ∼65 °C for ∼1 h. Following that, appropriate amounts of polymer-*g*-silica NPs were added. After mixing at the same temperature for another 1 h, the composite solutions were probe-ultrasonicated for 3 min using an ultrasonic processor (model GEX-750) operated at 24% of maximum amplitude with a pulse mode of 2 s sonication followed by 1 s rest. These solutions were poured into a PTFE Petri dish or drop-cast onto a glass slide. The solvent was removed by evaporation at either room conditions or ∼65 °C. The resulting nanocomposite films were air-dried in a fume hood for several days, then annealed at 80 °C in a vacuum oven for 24 h, and stored in a desiccator for further use (note that the 46 kg mol^{-1} PEO based samples were only annealed at 80 °C for 2 h to minimize the thermal degradation). Crystallization of the annealed films was conducted in either a water bath (IKA IB 20 pro) or a differential scanning calorimetry (DSC) at a specified temperature or cooling rate. When using a water bath, the samples (contained in a threaded, aluminum capsule tube with silica gel) were first heated to 85 °C in a vacuum oven, stabilized for half an hour, and then quickly transferred to the water bath, which had been equilibrated at the prespecified temperature. After crystallization, the aluminum tube was taken out from the water bath and cooled to room temperature.

Differential Scanning Calorimetry (DSC). Modulated DSC measurements were performed on a TA Q100 in a nitrogen atmosphere. The instrument was calibrated with indium for temperature and sapphire for heat capacity. All the experiments were conducted using a modulation amplitude of 1 °C and a modulation period of 60 s. Initially, 10−40 mg of the annealed sample was placed in an aluminum pan, heated to 100 °C, and stabilized for 10 min to erase any thermal history and prevent the self-seeding of PEO. For isothermal crystallization, the sample was first rapidly cooled down to 70 °C with an equilibration of 5 min, and then jumped to the preset temperature for isothermal crystallization. This two-step cooling procedure was used to mitigate the effect of temperature overshoot on isothermal crystallization.

Cross-Polarized Optical Microscopy (POM). Transmission POM, using an Olympus BX 50 microscope equipped with a movable heating plate provided by Linkam Ltd., was used to estimate the spherulite growth rate and from there the NP mobility at a specified crystallization temperature. A glass slide supported thin sample film, prepared according to the procedure described earlier, was first heated up to 90 °C for 10 min to erase the thermal history and to eliminate any self-seeding nuclei. The sample was then cooled down to the preset temperature for crystallization. Once the desired temperature was reached, a real-time video of the growing spherulites was recorded. The spherulite sizes at different crystallization times for each sample were then measured using ImageJ (version 1.45s), from which the spherulitic growth rates can be extracted. A copper wire with a known diameter was used to calibrate the magnification of the microscope.

Transmission/Scanning Electron Microscopy (TEM/SEM). Sections of 70−90 nm thickness were prepared using a Leica EM UC6 microtome operating at −120 °C with a Leica EM FC6 cryo attachment and a diamond knife. In some cases, the resulting thin sections were collected on copper TEM grids and quickly transferred to a liquid nitrogen container to minimize water absorption. Samples were stored in liquid nitrogen for less than a week. A cryo-transfer holder was used to load the frozen samples into a Tecnai G2 20 XTWIN electron microscope. The accelerating voltage was 200 kV, the sample temperature was −170 °C, and low dose (∼300 e$^-$/nm^2) was used to minimize beam damage. In other cases the thin sections were quickly transferred to a small plastic box containing silica gel particles to minimize water adsorption, and finally visualized in a JEOL JEM-100 CX electron microscope at room temperature. The fracture surface morphology of the specimens tested in the 3-point bending experiments was examined in a FEI Versa 3D scanning electron microscope using an accelerating voltage of 1−2 kV. To avoid charge accumulation on the sample surface during imaging, a thin layer of platinum (less than 1 nm) was deposited onto the specimen surface using a Technics Hummer V sputter coater.

Scattering Characterization. SAXS measurements were performed on beamline 12-ID-B at the Advanced Photon Source using a photon energy of 14 keV and a detector distance of 3.6 m (leading to a q range of 0.002−0.52 Å^{-1}, the beam size is 30 μm × 200 μm) or on a lab-scale X-ray setup (Bruker Nanostar U) at the Center for Functional Nanomaterials of Brookhaven National Laboratories with a q range of 0.0048−0.2 Å^{-1}. USAXS experiments were performed on the Bonse/Hart camera at the LIONS laboratory in CEA Saclay in France, covering a q range of 0.0003−0.09 Å^{-1}. Small angle neutron scattering (SANS) experiments were carried out on the GP-SANS beamline at HFIR at the Oak Ridge National Laboratory or the NGB 30m beamline at National Institute of Standards and Technology. The VSANS data were collected at the KWS-3 beamline at Heinz Maier-Leibnitz Zentrum in Germany. All samples were examined at room temperature unless otherwise indicated. XRD tests were performed using a PANalytical Xpert3 Powder X-ray diffractometer over the range of $5° < 2\theta < 60°$. Each sample was analyzed for 5 min at room temperature. The obtained Bragg peak at $2\theta \approx 19°$ was fit to a Pearson and Lorentz function to estimate its full width at half-maximum, from which the lamellar thickness (L_c) can be derived according to Scherrer's equation.

Mechanical Tests. Dynamic Mechanical Thermal Analysis (DMTA) was conducted on a Rheometrics Instruments DMTA-V using a sample dimension of ∼10 mm × 2.5 mm × 0.66 mm. All tests were performed at 25 °C in a tension mode at a strain of 0.01% to ensure that the loading was elastic. The probed frequency of deformation ranges from 0.002 to 100 Hz.

Single-edge notched 3-point bending (SEN-3PB) experiments were carried out to examine the fracture toughness of the testing specimens following ASTM standard D5045-14. The specimen geometry is approximately 38 mm × 6 mm × 2.5 mm, with a support span of 24 mm. Prior to tests, the surfaces of the specimens were first smoothened and then a precrack of a determined length was made with a fresh razor blade driven by a mill machine. The actual length of the precrack was ultimately determined by an optical microscope after the bending test. The fracture toughness was measured on an Instron 4204 mechanical testing machine using a miniature three point bend fixture (2810-412, Instron) at a constant displacement rate of 0.3 mm/min. Estimation of the stress intensity factor (K_{1q}) and the strain energy release rate (G_{1q})

DOI: 10.1021/acscentsci.7b00157
ACS Cent. Sci. 2017, 3, 751−758

was conducted following the ASTM standard D5045-14. For each material at a ligament length $l \sim 3$ mm, at least three specimens were tested to estimate G_{1q}. Note that, due to the limitation in the quantity of the materials, the sample geometry used in the current work does not strictly follow the plane strain criteria suggested by ASTM. However, our samples do satisfy the plane strain conditions defined by work of fracture for ductile materials.[31] Finally, the work of fracture for each specimen at different precrack lengths was determined by integration of the load−displacement curve.

Numerical Studies. We conducted molecular dynamics simulations on 40 NPs interacting with a pillar-like growing crystalline front in a simulation box with periodic boundary conditions in x- and y-directions (Figure 3A).[33] NP−NP interactions are purely repulsive corresponding to a truncated and shifted Lennard-Jones potential with energy constant $\varepsilon = 1.0$, particle diameter $\sigma = 1.0$, and cutoff distance $r_c = 2^{1/6}\sigma$. All parameters are in Lennard-Jones units. The van der Waals repulsion experienced by the NP at a distance d from the crystal (both on top and on the side) is $F_{vdW} = -\frac{2}{3}\frac{a^3AR}{4a+R}\left(\frac{1}{d}\right)^4$, $a = 0.002\sigma$ is the solvent size, $A = -0.4\varepsilon$ is the Hamaker constant, and R is the particle radius. The NPs also experience a Stokes viscous drag force according to the medium viscosity η and stochastic noise $\varsigma(t)$ modeled via Langevin dynamics. The particle equation of motion is $m\ddot{r} = -\frac{\partial H}{\partial r} - \Gamma\dot{r} + \varsigma(t)$, where H is the system Hamiltonian and the drag coefficient follows $\Gamma = 6\pi R\eta$. The particle trajectories are calculated forward in time via the velocity-Verlet algorithm. Here, it is important to discuss how kinetic engulfment and NP trajectories near the crystal front ($d < 0.05\sigma$) are evaluated. The NP can move away from the crystal if its velocity in the direction of crystallization is larger than G. Otherwise, particle motion stops and it is engulfed. NP organization results at low crystallization velocities ($G < G_c$). Interlamellar particles are located on the sides of the crystal, while interfibrillar NPs are placed on top of the growing front. Simulation data points correspond with averages over five runs.

■ ASSOCIATED CONTENT

Supporting Information

The Supporting Information is available free of charge on the ACS Publications website at DOI: 10.1021/acscentsci.7b00157.

Estimation of the PEO long period from the XRD data, additional modeling of modulus reinforcement, calculation of fracture toughness, tables, and figures (PDF)

■ AUTHOR INFORMATION

Corresponding Authors

*E-mail: jj2721@columbia.edu; jacques.jestin@cea.fr.
*E-mail: sk2794@columbia.edu.

ORCID

Vianney Gimenez-Pinto: 0000-0001-9789-2030
Andrew M. Jimenez: 0000-0001-7696-9705
Sanat K. Kumar: 0000-0002-6690-2221
Enrique D. Gomez: 0000-0001-8942-4480
Brian C. Benicewicz: 0000-0003-4130-1232

Notes

The authors declare no competing financial interest.

■ ACKNOWLEDGMENTS

The authors acknowledge financial support from National Science Foundation DMR-1408323 (D.Z., V.G.-P., A.M.J., S.K.K.) and DMR-1508249. This research used resources of the Advanced Photon Source, a U.S. Department of Energy (DOE) Office of Science User Facility operated for the DOE Office of Science by Argonne National Laboratory under Contract No. DE-AC02-06CH11357. We acknowledge the support of the National Institute of Standards and Technology, U.S. Department of Commerce, in providing the neutron research facilities used in this work. Additionally, this research used resources of the Center for Functional Nanomaterials, which is a U.S. DOE Office of Science Facility, at Brookhaven National Laboratory under Contract No. DE-SC0012704. A portion of this research at ORNL's High Flux Isotope Reactor was sponsored by the Scientific User Facilities Division, Office of Basic Energy Sciences, US Department of Energy. We would like to thank Linxi Zhang and Dr. Chung-Chueh Chang for help with cryo-TEM imaging. Dr. Oleg Gang, Dmytro Nykypanchuk, Suchetan Pal, Xiaobing Zuo, and Dr. Olivier Taché are acknowledged for help in SAXS and USAXS measurements, respectively. The SANS and VSANS measurements were conducted with the assistance of Dr. Markus Bleuel and Dr. Vitaliy Pipich. We would also like to thank Arthur J. Autz for help in preparation of the prenotched samples for SEN-3PB tests and Prof. Jeffrey W. Kysar for help in toughness measurements. The authors thank Dr. Jack Douglas, Dr. Guruswamy Kumaraswamy, Dr. Sylvain Deville, Prof. Thomas Russell, Prof. Mary Boyce, Dr. George Floudas, Dr. Richard A. Vaia, Prof. James Runt, and Prof. Michael Rubinstein for many useful discussions and also for comments on this manuscript.

■ REFERENCES

(1) Tao, J.; Pan, H.; Zeng, Y.; Xu, X.; Tang, R. Roles of amorphous calcium phosphate and biological additives in the assembly of hydroxyapatite nanoparticles. *J. Phys. Chem. B* **2007**, *111*, 13410−13418.

(2) Cai, Y.; Tang, R. Calcium phosphate nanoparticles in biomineralization and biomaterials. *J. Mater. Chem.* **2008**, *18*, 3775−3787.

(3) Moll, J. F.; Akcora, P.; Rungta, A.; Gong, S.; Colby, R. H.; Benicewicz, B. C.; Kumar, S. K. Mechanical reinforcement in polymer melts filled with polymer grafted nanoparticles. *Macromolecules* **2011**, *44*, 7473−7477.

(4) Chen, L.-Y.; Xu, J.-Q.; Choi, H.; Pozuelo, M.; Ma, X.; Bhowmick, S.; Yang, J.-M.; Mathaudhu, S.; Li, X.-C. Processing and properties of magnesium containing a dense uniform dispersion of nanoparticles. *Nature* **2015**, *528*, 539−543.

(5) Balazs, A. C.; Emrick, T.; Russell, T. P. Nanoparticle Polymer Composites: Where Two Small Worlds Meet. *Science* **2006**, *314*, 1107−1110.

(6) Mackay, M. E.; Tuteja, A.; Duxbury, P. M.; Hawker, C. J.; Van Horn, B.; Guan, Z.; Chen, G.; Krishnan, R. S. General strategies for nanoparticle dispersion. *Science* **2006**, *311*, 1740−1743.

(7) Kakisawa, H.; Sumitomo, T. The toughening mechanism of nacre and structural materials inspired by nacre. *Sci. Technol. Adv. Mater.* **2011**, *12*, 064710.

(8) Sumitomo, T.; Kakisawa, H.; Owaki, Y.; Kagawa, Y. Transmission electron microscopy observation of nanoscale deformation structures in nacre. *J. Mater. Res.* **2008**, *23*, 3213−3221.

(9) Deville, S. Freeze-casting of porous ceramics: a review of current achievements and issues. *Adv. Eng. Mater.* **2008**, *10*, 155−169.

(10) Deville, S.; Saiz, E.; Nalla, R. K.; Tomsia, A. P. Freezing as a path to build complex composites. *Science* **2006**, *311*, 515−518.

DOI: 10.1021/acscentsci.7b00157
ACS Cent. Sci. 2017, 3, 751−758

(11) Deville, S.; Saiz, E.; Tomsia, A. P. Ice-templated porous alumina structures. *Acta Mater.* **2007**, *55*, 1965−1974.
(12) Cai, J.; Lv, C.; Watanabe, A. Facile preparation of hierarchical structures using crystallization-kinetics driven self-assembly. *ACS Appl. Mater. Interfaces* **2015**, *7*, 18697−18706.
(13) Finnemore, A.; Cunha, P.; Shean, T.; Vignolini, S.; Guldin, S.; Oyen, M.; Steiner, U. Biomimetic layer-by-layer assembly of artificial nacre. *Nat. Commun.* **2012**, *3*, 966.
(14) Sellinger, A.; Weiss, P. M.; Nguyen, A.; Lu, Y.; Assink, R. A.; Gong, W.; Brinker, C. J. Continuous self-assembly of organic−inorganic nanocomposite coatings that mimic nacre. *Nature* **1998**, *394*, 256−260.
(15) Hoffman, J. D.; Miller, R. L. Kinetic of crystallization from the melt and chain folding in polyethylene fractions revisited: theory and experiment. *Polymer* **1997**, *38*, 3151−3212.
(16) Barr, S. A.; Luijten, E. Structural properties of materials created through freeze casting. *Acta Mater.* **2010**, *58*, 709−715.
(17) Körber, C.; Rau, G.; Cosman, M.; Cravalho, E. Interaction of particles and a moving ice-liquid interface. *J. Cryst. Growth* **1985**, *72*, 649−662.
(18) Keith, H.; Padden, F., Jr Spherulitic crystallization from the melt. I. Fractionation and impurity segregation and their influence on crystalline morphology. *J. Appl. Phys.* **1964**, *35*, 1270−1285.
(19) Mackay, M. E.; Dao, T. T.; Tuteja, A.; Ho, D. L.; Van Horn, B.; Kim, H.-C.; Hawker, C. J. Nanoscale effects leading to non-Einstein-like decrease in viscosity. *Nat. Mater.* **2003**, *2*, 762−766.
(20) Kalathi, J. T.; Yamamoto, U.; Schweizer, K. S.; Grest, G. S.; Kumar, S. K. Nanoparticle diffusion in polymer nanocomposites. *Phys. Rev. Lett.* **2014**, *112*, 108301.
(21) Teramoto, A.; Fujita, H. Temperature and molecular weight dependence of the melt viscosity of polyethylene oxide in bulk. *Makromol. Chem.* **1965**, *85*, 261−272.
(22) Talibuddin, S.; Wu, L.; Runt, J.; Lin, J. Microstructure of melt-miscible, semicrystalline polymer blends. *Macromolecules* **1996**, *29*, 7527−7535.
(23) Ito, H.; Russell, T.; Wignall, G. Interactions in mixtures of poly(ethylene oxide) and poly(methyl methacrylate). *Macromolecules* **1987**, *20*, 2213−2220.
(24) Pedemonte, E.; Burgisi, G. Thermodynamics of poly (ethylene oxide)-poly (methyl acrylate) blends: prediction of miscibility based on the Prigogine-Flory theory. *Polymer* **1994**, *35*, 3719−3721.
(25) Khan, J.; Harton, S. E.; Akcora, P.; Benicewicz, B. C.; Kumar, S. K. Polymer crystallization in nanocomposites: spatial reorganization of nanoparticles. *Macromolecules* **2009**, *42*, 5741−5744.
(26) Uhlmann, D. R.; Chalmers, B.; Jackson, K. Interaction between particles and a solid-liquid interface. *J. Appl. Phys.* **1964**, *35*, 2986−2993.
(27) Russell, T.; Ito, H.; Wignall, G. Neutron and x-ray scattering studies on semicrystalline polymer blends. *Macromolecules* **1988**, *21*, 1703−1709.
(28) Rajamanickam, R.; Kumari, S.; Kumar, D.; Ghosh, S.; Kim, J. C.; Tae, G.; Sen Gupta, S.; Kumaraswamy, G. Soft colloidal scaffolds capable of elastic recovery after large compressive strains. *Chem. Mater.* **2014**, *26*, 5161−5168.
(29) Guth, E. Theory of filler reinforcement. *J. Appl. Phys.* **1945**, *16*, 20−25.
(30) Wei, G.-X.; Sue, H.-J.; Chu, J.; Huang, C.; Gong, K. Toughening and strengthening of polypropylene using the rigid−rigid polymer toughening concept Part I. Morphology and mechanical property investigations. *Polymer* **2000**, *41*, 2947−2960.
(31) Wu, J.; Mai, Y. W. The essential fracture work concept for toughness measurement of ductile polymers. *Polym. Eng. Sci.* **1996**, *36*, 2275−2288.
(32) Li, C.; Han, J.; Ryu, C. Y.; Benicewicz, B. C. A versatile method to prepare RAFT agent anchored substrates and the preparation of PMMA grafted nanoparticles. *Macromolecules* **2006**, *39*, 3175−3183.
(33) Plimpton, S. Fast parallel algorithms for short-range molecular dynamics. *J. Comput. Phys.* **1995**, *117*, 1−19.

DOI: 10.1021/acscentsci.7b00157
ACS Cent. Sci. 2017, 3, 751−758